Structural Modifications in Vitreous SiO_2 Induced by N and Ar Ion Irradiation: Competing Roles of Nuclear and Electronic Energy Losses

N. Cheridi and A. Meftah*

LRPCSI, Faculty of Sciences, Université 20 août 1955-Skikda, 21000 Skikda, Algeria

Received: 30.04.2025 & Accepted: 23.07.2025

Doi: 10.12693/APhysPolA.148.34 *e-mail: a.meftah@univ-skikda.dz

This study investigated structural modifications in vitreous silica (SiO_2) induced by low-energy ion irradiation using 75 keV N^{5+} and 165 keV Ar^{11+} ions. The primary goal was to clarify the competing roles of nuclear and electronic energy losses in these changes. Fourier transform infrared spectroscopy revealed a decrease in the 1078 cm^{-1} TO3 band and the appearance of a 1044 cm^{-1} peak, indicating bond angle distortion and densification. Comparative analysis, supported by the unified thermal spike model, demonstrates that nuclear energy loss is the dominant mechanism driving structural transformations under these irradiation conditions, with electronic energy loss having a limited impact.

topics: vitreous silica, ion irradiation, structural modifications, infrared spectroscopy

1. Introduction

Vitreous silica (SiO_2), prized for its superior mechanical, optical, chemical, and electrical properties, is a crucial material in high-technology sectors, especially those involving exposure to ionizing radiation, such as nuclear and spatial applications. Understanding how radiation alters the structure of vitreous silica is therefore vital for ensuring the longevity and efficacy of these technologies. Although the literature contains extensive studies on defect formation in SiO_2 under ion bombardment [1–8], the relative importance of nuclear and electronic energy losses (i.e., S_n and S_e, respectively) in driving these changes remains an open question, particularly at low ion energies (as those used in this paper — 75 keV N^{5+} and 165 keV Ar^{11+}). To address this, our research uniquely integrates detailed infrared spectroscopy measurements, which provide insights into the Si–O–Si bond angle and network modifications, with theoretical simulations based on the unified thermal spike model (u-TSM). This combined approach aims to establish a direct link between the energy deposited through both nuclear and electronic processes and the resulting structural transformations, ultimately identifying the dominant energy loss mechanism responsible for damage in SiO_2 under these specific irradiation conditions.

2. Experimental methodology

Thin films of vitreous SiO_2 (approximately 104 nm thick, with mass density of 2.2 g/cm^3) were thermally grown on both sides of 5 cm diameter Si (100) wafers. Samples ($\simeq 1 \times 1$ cm^2) were cut and irradiated at normal incidence with 75 keV N^{5+} and 165 keV Ar^{11+} ions at ARIBE (Accélérateur pour la Recherche avec des Ions de Basse Énergie,

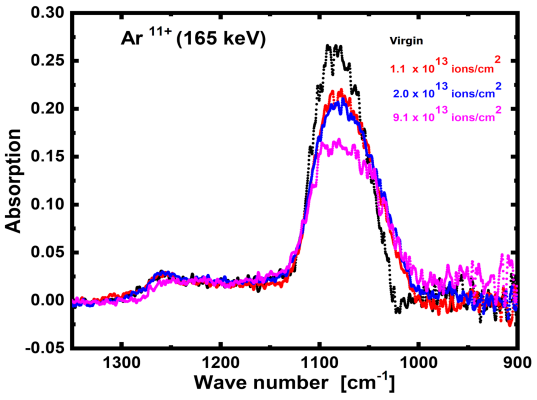

Fig. 1. Infrared spectra of vitreous SiO_2 in the 900–1350 cm^{-1} range following irradiation with 165 keV Ar^{11+} ion at the indicated fluences.

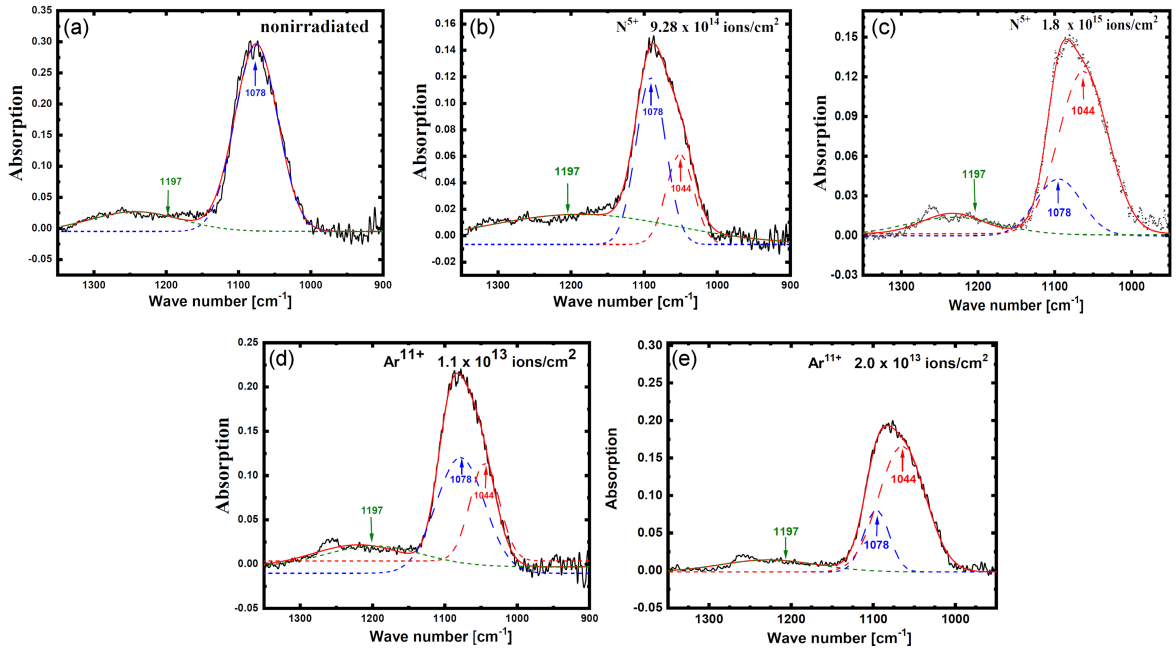

Fig. 2. Infrared spectra of vitreous SiO_2: (a) unirradiated, (b, c) irradiated with 75 keV N^{5+} ions, and (d, e) irradiated with 165 keV Ar^{11+} ions at the indicated fluences. The dashed lines represent the fitted contributions of the 1044, 1078, and 1197 cm^{-1} bands (labeled in the figure). The red solid line shows the sum of these fitted bands, plotted against the experimental data (black dots).

CIMAP, GANIL, Caen, France). These specific ions and energies were chosen because of their comparable nuclear and electronic energy losses, allowing for a direct comparison of their effects. The estimated energy loss values, calculated using the Stopping and Range of Ions in Matter (SRIM) code [9], are summarized below:

- For 75 keV N^{5+} ions, the electronic energy loss is $S_e = 260$ eV/nm, the nuclear energy loss is $S_n = 80$ eV/nm, and the projected range is $R_p = 210$ nm.
- For 165 keV Ar^{11+} ions, the electronic energy loss is $S_e = 390$ eV/nm, the nuclear energy loss is $S_n = 420$ eV/nm, and the projected range is $R_p = 175$ nm.

Ion fluxes ranged from 1×10^{10} to 6×10^{10} ions/(cm^2 s), with fluences up to 3×10^{15} ions/cm^2. Structural changes were monitored by Fourier transform infrared (FTIR) spectroscopy using a Nicolet iS10 spectrometer operating at a resolution of 2 cm^{-1} over 64 scans.

3. Results and discussion

3.1. Infrared spectroscopy

Figure 1 illustrates the evolution of infrared spectra with increasing ion fluence for vitreous SiO_2 samples irradiated with 165 keV Ar^{11+} ions. The analysis concentrated on the TO3 absorption band (1000–1120 cm^{-1}) and the LO4–TO4 pair (1165–1200 cm^{-1}). The primary observations were as follows:

- There was a decrease in the intensity of the 1078 cm^{-1} TO3 band, accompanied by the appearance of a peak at 1044 cm^{-1}, indicating a reduction in the Si–O–Si bond angle and a consequent compaction.
- The intensity of the LO4–TO4 band remained largely unchanged.

The full width at half maximum (FWHM) values of the bands at 1078, 1197, and 1044 cm^{-1} were obtained by Gaussian fitting. These values are consistent with previously reported data [5, 7]. The Gaussian fits are shown in Fig. 2, which displays the infrared spectra of unirradiated samples as well as those irradiated at various fluences with both N^{5+} and Ar^{11+} ions.

3.2. Cross-section of structural transformation and radius determination

The increases in the peak area of the 1044 cm^{-1} band as a function of ion fluence (for 75 keV N^{5+} and 165 keV Ar^{11+} ions) are shown in Fig. 3. At high fluences, saturation behavior is observed — the 1044 cm^{-1} band reaches a maximum. At low fluences, the increase in the 1044 cm^{-1} band (associated with disordered SiO_2) is proportional to the

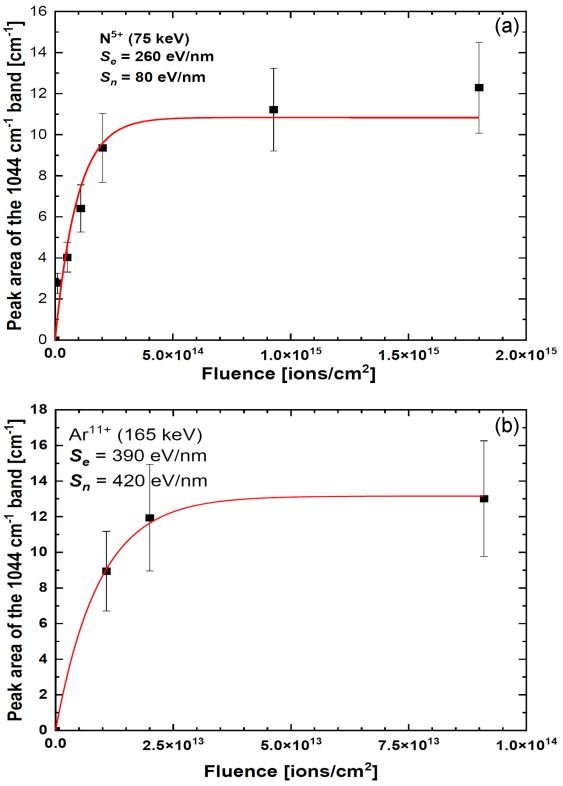

Fig. 3. Evolution of the 1044 cm^{-1} band area with ion fluence for irradiation with 75 keV N^{5+} and 165 keV Ar^{11+} ions. Solid lines represent fits to the experimental data using Poisson's law.

absorbed dose. The evolution of the band area with fluence ϕ is shown in Fig. 3 and fitted using Poisson's law [10]

$$F_d = 1 - \exp(-\sigma\phi), \tag{1}$$

where F_d is the fraction of the damaged material, and σ is the effective damage cross-section for the structural transformation.

Now, F_d is defined as $F_d = N/N_0$, where N is the number of oscillators associated with the newly formed absorption band induced by irradiation, and N_0 corresponds to the number of oscillators at complete damage. Since the number of oscillators is proportional to the area of the absorption band, F_d can be directly related to the ratio of band areas.

Therefore, F_d can also be expressed as $F_d = S/S_0$, where S represents the area of the irradiation-induced absorption band at a given fluence, and S_0 is the saturation value corresponding to the complete damage of the material. The evolution of the irradiation-induced peak (Fig. 3) will be analyzed using the following relation

$$S = S_0\left(1 - \exp(-\sigma\varphi)\right). \tag{2}$$

The variation of the induced peak area as a function of fluence enables the estimation of both the initial slope and the damage cross-section, and consequently, the effective damage radius. The initial slope of this curve (see Fig. 3) provides insight into the damage efficiency in the low-fluence regime, where track overlapping is negligible. It is determined by evaluating the derivative of the fluence-dependent function at zero fluence.

Assuming that each ion produces a circular damage track, the effective damage radius R can be calculated using the relation $\sigma = \pi R^2$. The calculated damage cross-section σ and radii R for irradiations with N^{5+} and Ar^{11+} ions are given in Table I.

TABLE I

Deduced and modeled damage radii for N and Ar ion irradiation. The table presents: ion energy (E), electronic (S_e) and nuclear (S_n) energy losses (calculated using the SRIM code [9]), experimentally determined damage radius (R_{exper}), and damage radius (R_{model}) predicted by the unified thermal spike model.

Parameter	Ion	
	N^{5+}	Ar^{11+}
E [keV]	75	165
S_e [eV/nm]	260	390
S_n [eV/nm]	80	420
σ [cm^2]	$(1.1 \pm 0.4) \times 10^{-14}$	$(1.1 \pm 0.7) \times 10^{-13}$
R_{exper} [nm]	0.6 ± 0.2	1.9 ± 0.4
R_{model} [nm]	0.6	1.6

3.3. Unified thermal spike model (u-TSM) analysis

A unified thermal spike model (u-TSM) was employed to interpret the experimental results. This model, detailed by Mieskes et al. [11] and Toulemonde et al. [7], integrates the elastic collision spike and inelastic thermal spike models to account for both nuclear and electronic energy losses. It describes the diffusion of electronic energy loss via electron–electron interactions and its subsequent transfer to the lattice through electron–phonon coupling. Nuclear energy, in contrast, is deposited directly onto the atoms, leading to a transient thermal effect, as proposed by Ollerhead et al. [12]. The thermal spike model [13–16] is a widely used and effective tool for describing swift heavy ion-induced damage in various materials, including metals [17], semiconductors [18], and insulators [19–21]. The model is governed by the following coupled differential equations

$$C_e(T_e)\frac{\partial T_e}{\partial t} = \frac{1}{r}\frac{\partial}{\partial r}\left(rK_e(T_e)\frac{\partial T_e}{\partial r}\right) - g(T_e - T_a) + A_e(r,t), \tag{3}$$

$$C_a(T_a)\frac{\partial T_a}{\partial t} = \frac{1}{r}\frac{\partial}{\partial r}\left(rK_a(T_a)\frac{\partial T_a}{\partial r}\right) + g(T_e - T_a) + B_n(r,t). \tag{4}$$

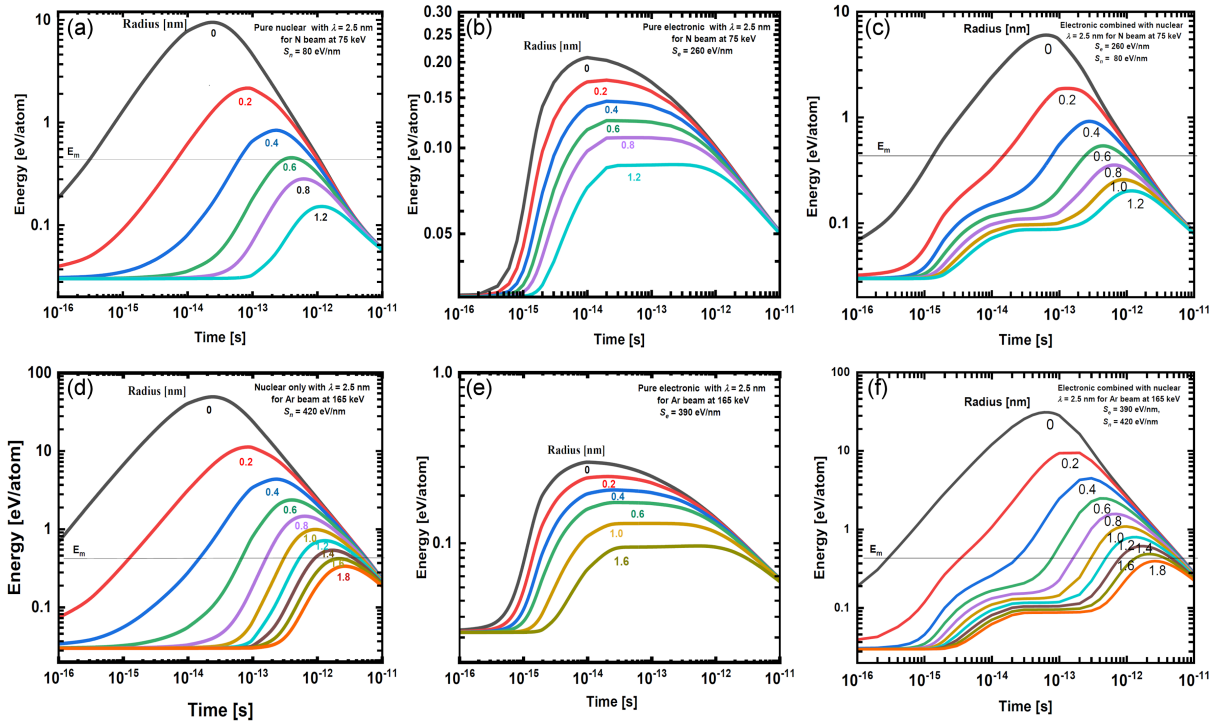

Fig. 4. Time evolution of energy transferred to atoms at various radial distances [nm] from the ion path for N^{5+} and Ar^{11+} ions. Curves show contributions from pure nuclear energy loss (S_n), pure electronic energy loss (S_e), and their combination (S_{total}), as indicated. U-TSM calculations were performed with $\lambda = 2.5$ nm. For nitrogen irradiation (a, c), the melting energy threshold ($E_m = 0.38$ eV/at) is exceeded within a radius of 0.6 nm. Under argon irradiation (d, f), this threshold is surpassed within a radius of 1.6 nm.

Here, T_e and T_a represent the electronic and atomic temperatures, respectively, while C_e and C_a are their corresponding specific heats. Further, K_e and K_a denote the thermal conductivities, and g is the electron–phonon coupling constant.

In (3), $A_e(r,t)$ represents the energy transferred to the electronic subsystem by the incident ion through ballistic collisions at a radius r. Integrating $A_e(r,t)$ over space yields the electronic stopping power (S_e). Conversely, $B_n(r,t)$ in (4) accounts for the additional energy contribution from nuclear energy deposition [22]. This term is significant in the formation of a molten zone [23], indicating the energy input into the atomic system.

These two equations, i.e., (3) and (4), are solved numerically to account for the evolution of all parameters with respect to T_e and T_a. The electron–phonon coupling constant g, which is the only free parameter of the model, is related to the electron–phonon mean free path λ by the expression

$$\lambda^2 = D_e C_e / g, \tag{5}$$

as proposed for insulators [24]. Here, D_e and C_e represent the electronic thermal diffusivity and the electronic specific heat, respectively, and are treated as constants for insulators ($C_e = 1$ J/(g K) [25], $D_e = 2$ cm^2/s [25, 26]). The parameter λ characterizes the radial expansion of the initial energy before it is transfered to the atoms. This model is applicable because the high charge of the incident ion is neutralized within a depth of less than 5 nm [27].

Model simulations were performed assuming a superheating scenario [15, 28]. In these simulations, track radii were defined by the regions where the deposited energy surpassed the melting energy threshold ($E_m = 0.38$ eV/atom for vitreous SiO_2). An electron–phonon mean free path (λ) of 2.5 nm was used in the model. This parameter characterizes the characteristic radial distance over which the electronic energy initially deposited by the ion spreads before being transferred to the lattice via electron–phonon interactions. The value of 2.5 nm corresponds to the best-fit parameter determined by Toulemonde et al. [29].

Figure 4 illustrates the temporal evolution of atomic energy deposition at various radial distances. The key findings include:

- For 75 keV N^{5+} ions, despite nuclear energy loss being three times lower than electronic energy loss, the thermal effect from nuclear collisions is at least ten times greater than that from electronic collisions.
- In the case of 165 keV Ar^{11+} ions, where nuclear and electronic energy losses are comparable, nuclear energy loss remains the dominant factor in structural modifications.

- These findings confirm that at low irradiation energies, structural modifications in vitreous SiO_2 are primarily driven by nuclear energy loss, with negligible contributions from electronic excitation, even for light incident ions.

4. Conclusions

This study provides compelling evidence that nuclear energy loss is the primary driver of structural modifications in vitreous SiO_2 under low-energy ion irradiation. The observed spectroscopic signatures — specifically the attenuation of the 1078 cm^{-1} band coupled with the emergence of the 1044 cm^{-1} peak — strongly indicate a reduction in the Si–O–Si bond angle, resulting in material compaction, which is consistent with previous research [5, 7]. The successful application of the unified thermal spike model (u-TSM) further reinforces these findings, unequivocally demonstrating the negligible contribution of electronic excitation to structural changes at these energy levels. The results hold significant implications for the design of radiation-hardened materials, particularly in environments where low-energy ion bombardment is prevalent. Furthermore, the understanding gained here is crucial for optimizing the long-term performance of materials used in nuclear waste containment, where resistance to radiation-induced structural alterations is paramount.

Acknowledgments

The authors thank Dr. M. Toulemonde for his insightful discussions and support during the experimental campaign at CIMAP, GANIL, Caen, France.

References

[1] A. Benyagoub, S. Löffler, M. Rammensee, S. Klaumünzer, G. Saemannn-Ischenko, *Nucl. Instrum. Methods Phys. Res. B* **65**, 228 (1992).

[2] M.C. Busch, A. Slaoui, P. Siffert, E. Dooryhee, M. Toulemonde, *J. Appl. Phys.* **71**, 2596 (1992).

[3] A. Meftah, M. Djebara, N. Khalfaoui, M. Toulemonde, *Nucl. Instrum. Methods Phys. Res. B* **146**, 431 (1998).

[4] S. Klaumünzer, *Nucl. Instrum. Methods Phys. Res. B* **225**, 136 (2004).

[5] C. Rotaru, F. Pawlak, N. Khalfaoui, C. Dufour, J. Pérričre, A. Laurent, J.P. Stoquert, H. Lebius, M. Toulemonde, *Nucl. Instrum. Methods Phys. Res. B* **272**, 9 (2012).

[6] K. Awazu, S. Ishii, K. Shima, S. Roorda, J.L. Brebner, *Phys. Rev. B* **62**, 3689 (2000).

[7] M. Toulemonde, W.J. Weber, G.S. Li, V. Shutthanandan, P. Kluth, T. Yang, Y. Wang, Y. Zhang, *Phys. Rev. B* **83**, 054106 (2011).

[8] A. Benyagoub, M. Toulemonde, *J. Mater. Res.* **30**, 1529 (2015).

[9] J.P. Biersack, L.G. Haggmark, *Nucl. Instrum. Methods* **174**, 257 (1980).

[10] P. Thévenard, G. Guiraud, C.H.S. Dupuy, B. Delaunay, *Radiat. Eff.* **32**, 83 (1977).

[11] H.D. Mieskes, W. Assmann, F. Grüner, H. Kucal, Z.G. Wang, M. Toulemonde, *Phys. Rev. B* **67**, 155414 (2003).

[12] J.P. Ollerhead, J. Bottiger, J.A. Davies, J. L'ecuyer, H.K. Haugen, N. Matsunami, *Radiat. Eff.* **49**, 203 (1980).

[13] M. Toulemonde, C. Dufour, E. Paumier, F. Pawlak, *MRS Proc.* **504**, 99 (1998).

[14] A. Benyagoub, S. Klaumünzer, M. Toulemonde, *Nucl. Instrum. Methods Phys. Res. B* **146**, 449 (1998).

[15] A. Dallanora, T.L. Marcondes, G.G. Bermudez, P.F.P. Fichtner, C. Trautmann, M. Toulemonde, R.M. Papaléo, *J. Appl. Phys.* **104**, 024307 (2008).

[16] M. Toulemonde, W. Assmann, C. Dufour, A. Meftah, F. Studer, C. Trautmann, in: *Ion Beam Science: Solved and Unsolved Problems*, Ed. P. Sigmund, The Royal Danish Academy of Sciences and Letters, Copenhagen 2006, p. 263.

[17] Z.G. Wang, C. Dufour, E. Paumier, M. Toulemonde, *J. Phys. Condens. Matter* **6**, 6733 (1994).

[18] M. Toulemonde, C. Dufour, E. Paumier, *Phys. Rev. B* **46**, 14362 (1992).

[19] A. Meftah, F. Brisard, J.M. Costantini et al., *Phys. Rev. B* **49**, 12457 (1994).

[20] A. Meftah, J.M. Costantini, N. Khalfaoui, S. Boudjadar, J.P. Stoquert, F. Studer, M. Toulemonde, *Nucl. Instrum. Methods Phys. Res. B* **237**, 563 (2005).

[21] M. Toulemonde, J.M. Costantini, C. Dufour, A. Meftah, E. Paumier, F. Studer, *Nucl. Instrum. Methods Phys. Res. B* **116**, 37 (1996).

[22] P. Sigmund, C. Claussen, *J. Appl. Phys.* **52**, 990 (1981).

[23] K. Nordlund, J. Peltola, J. Nord, J. Keinone, R.S. Averback, *J. Appl. Phys.* **90**, 1710 (2001).

[24] M. Toulemonde, C. Dufour, A. Meftah, E. Paumier, *Nucl. Instrum. Methods Phys. Res. B* **166–167**, 903 (2000).

[25] C. Dufour, A. Audouard, F. Beuneu et al., *J. Phys. Condens. Matter* **5**, 4573 (1993).

[26] Yu.V. Martynenko, Yu.N. Yavlinskii, *Sov. Phys. Dokl.* **2**, 391 (1983).

[27] C. Dufour, V. Khomrenkov, Y.Y. Wang, Z.G. Wang, F. Aumayr, M. Toulemonde, *J. Phys. Condens. Matter* **29**, 095001 (2017).

[28] M. Toulemonde, W. Assmann, C. Trautmann, F. Grüner, *Phys. Rev. Lett.* **88**, 057602 (2002).

[29] M. Toulemonde, W. Assmann, C. Trautmann, *Nucl. Instrum. Methods Phys. Res. B* **379**, 2 (2016).